

# R-curve of La<sub>2</sub>O<sub>3</sub> doped Zirconia Toughened Alumina Composites Prepared via Stereolithography based 3D Printing

**Haidong Wu**

Guangdong University of Technology

**W. Liu** (✉ [317127238@qq.com](mailto:317127238@qq.com))

Guangdong University of Technology

**Meipeng Huang**

Guangdong University of Technology

**Jianwei Liang**

Guangdong University of Technology

**Di An**

Tsinghua University

**Hezhen Li**

University of Science and Technology of Beijing

**Chengyong Wang**

Guangdong University of Technology

**Zhipeng Xie**

Tsinghua University

**Shanghua Wu** (✉ [swu@gdut.edu.cn](mailto:swu@gdut.edu.cn))

Guangdong University of Technology

---

## Research Article

**Keywords:** 3D printing, Stereolithography, R-curve, Doping, Toughening

**Posted Date:** April 16th, 2020

**DOI:** <https://doi.org/10.21203/rs.3.rs-22641/v1>

**License:**  This work is licensed under a Creative Commons Attribution 4.0 International License.

[Read Full License](#)

---

# Abstract

In this study, we combined liquid precursor infiltration of high introduction amounts of bi-additives (20wt%) and stereolithography-based 3D printing to fabricate zirconia toughened alumina, and the infiltration systems consist of the four following systems Zr<sup>4+</sup>/La<sup>3+</sup>, Zr<sup>4+</sup>/Er<sup>3+</sup>, Zr<sup>4+</sup>/Gd<sup>3+</sup>, and Zr<sup>4+</sup>/Ce<sup>4+</sup>. The sample immersed with Zr<sup>4+</sup>/La<sup>3+</sup> shows intense peaks of m-ZrO<sub>2</sub> phase compared to the other samples while a new phase of flake-like LaAl<sub>11</sub>O<sub>18</sub> occurs in the Zr<sup>4+</sup>/La<sup>3+</sup> immersed sample, the existence of which could be confirmed by XRD and EDS. The fracture toughness of the Zr<sup>4+</sup>/Er<sup>3+</sup>, Zr<sup>4+</sup>/Gd<sup>3+</sup>, and Zr<sup>4+</sup>/Ce<sup>4+</sup> samples remained basically unchanged versus the crack size, while the measured fracture toughness values for the Zr<sup>4+</sup>/La<sup>3+</sup> system could be fitted as a rising R-curve behavior with the steady-state fracture toughness of 17.76 MPa·m<sup>1/2</sup>. The enormous enhancement of the toughness could be attributed to thermal expansion misfit and flake-like LaAl<sub>11</sub>O<sub>18</sub> in the Zr<sup>4+</sup>/La<sup>3+</sup> system. The effect of residual stresses on the fracture mode and thus the toughness is discussed on the basis of theoretical calculation and analysis. It is the first time a rising R-curve behavior is observed in the 3D printed ceramics. The shocking discovery provides a highly effective toughening way in 3D printing combined infiltration approach.

## 1. Introduction

Zirconia toughened alumina (ZTA) ceramic has been used in many important engineering fields due to its high strength, high hardness, and good chemical corrosion resistance [1–2]. However, two major drawbacks greatly limit its application: One is the high hardness and strength of ZTA ceramic materials, which makes it hard to shape and process highly precise and highly complicated ceramic parts. The other is that the mechanical properties of Al<sub>2</sub>O<sub>3</sub> ceramics strengthened and toughened by mono phase are still need to be improved. For the preparation of ZTA ceramics, traditional methods such as dry pressing, cold isostatic pressing, slip casting, and injection molding [3–6] are all relied on mold-based manufacturing approaches which result in high costs and long production cycles while some certain special shapes and features are difficult or even impossible to produce. These limitations have placed significant constraints on the promotion and application of high-end equipment and key components. 3D printing (Additive manufacturing) is now gradually becoming substitutes of conventional shaping methods in some fields due to its feasibility of solving the aforementioned issues. Among the methods of 3D printing, stereolithography (SLA) has become the most popular method in ceramic 3D printing due to its high shaping speed, high shaping precision, and high density of green body, which could finally lead to high density and high performance ceramic parts [7–11].

The effect of multi-dopants toughening is better than mono-dopant, which has been evidenced in many literatures [12–13, 3]. For example, Y<sub>2</sub>O<sub>3</sub>, CeO<sub>2</sub>, SiC, and CNT were added as the second toughening phase in ZTA ceramics and the fracture toughness were significantly improved [13, 14–16]. In this study, four rare earth oxides were adopted as the second toughening phase in ZTA to conduct a systematic research to understand rare earth oxide-ZrO<sub>2</sub> integrated toughening behavior. The introduction approach of the bi-additives is liquid precursor immersion and the shaping method is 3D printing. It is the first time

that a rising R-curve behavior could be observed in 3D printed ceramics composites, i. e. the enormous enhancement of the crack resistance versus the crack size could be attributed to flake-like  $\text{LaAl}_{11}\text{O}_{18}$  in the  $\text{Zr}^{4+}/\text{La}^{3+}$  system. The shocking discovery provides a highly effective toughening way in the 3D printing combined liquid precursor infiltration approach.

## 2. Materials And Methods

The preparation of pre-sintered alumina samples can be found in our previous work [9]. The bi-additive systems consist of  $\text{Zr}^{4+}/\text{La}^{3+}$ ,  $\text{Zr}^{4+}/\text{Er}^{3+}$ ,  $\text{Zr}^{4+}/\text{Gd}^{3+}$ , with the molar ratio of 98:4, while an optimal composition of  $\text{Zr}^{4+}/\text{Ce}^{4+}$  with the molar ratio of 88:12 was adopted according to previous literature [17]. Solution A (2 mol% $\text{La}_2\text{O}_3$ - $\text{ZrO}_2$ ), solution B (2 mol% $\text{Er}_2\text{O}_3$ - $\text{ZrO}_2$ ), solution C (2 mol% $\text{Gd}_2\text{O}_3$ - $\text{ZrO}_2$ ), and solution D (12 mol% $\text{CeO}_2$ - $\text{ZrO}_2$ ) were prepared by dissolving analytically pure  $\text{ZrOCl}_2 \cdot 8\text{H}_2\text{O}$ , combined with  $\text{La}(\text{NO}_3)_3 \cdot 6\text{H}_2\text{O}$ ,  $\text{Er}(\text{NO}_3)_3 \cdot 5\text{H}_2\text{O}$ ,  $\text{Gd}(\text{NO}_3)_3 \cdot 6\text{H}_2\text{O}$ ,  $\text{Ce}(\text{NO}_3)_4 \cdot 6\text{H}_2\text{O}$ , and in deionized water, respectively. The Infiltration was conducted by immersing the alumina green body in solution at room temperature and ambient pressure. Then, the samples mentioned above were completely immersed in solution A, B, C and D at room temperature for 3 h, respectively. After the infiltration, the green parts were first cleaned with tissue to remove the residual solution and then immersed in an ammonia solution for 15 min. Finally, the green parts after immersing in an ammonia solution were dried in an oven at 60 °C for 12 h. All infiltration steps repeated for five times. All infiltration specimens were sintered at 1600°C for 1 h in a furnace (Thermconcept, HTK 16/18, Germany).

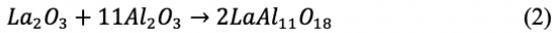
The weight of the second phase was calculated by comparing the green body before infiltration with the sintered body after infiltration. The density of the prepared alumina bodies was determined employing the Archimedes' principle using a balance with an accuracy of 0.0001 g. The Vickers hardness was tested using a Vickers hardness testing machine (HVS-30Z, Shanghai Precision Instrument Co., Ltd., China) by applying a load of 98 N after 10 s. The fracture toughness was also measured by indentation method applying the respective load of 49, 98, 196, 294 N after 10 s. The fracture toughness was assessed by measuring the crack lengths produced by the Vickers indentation tests. The fracture toughness was then calculated using the following equation proposed by Niihara [18]

$$K_{Ic} = \frac{0.035}{3} \left(\frac{l}{a}\right)^{-\frac{1}{2}} H \sqrt{a} \left(\frac{H}{3E}\right)^{-0.4} \quad (1)$$

where H is the hardness, a is half length of the indentation diagonal, l is the length of the crack propagation, E is the elastic modulus. At least 5 indentation tests were performed for each sample at randomly chosen spots. The radial crack lengths were measured using an optical microscope. The phase compositions of the prepared ceramic parts were determined by X-ray diffraction (XRD, Bruker D8, Germany), and the microstructures of the sintered body were characterized by scanning electron microscopy (SEM, Nova NanoSEM 430, FEI, Netherlands).

### 3. Results And Discussion

The microstructures of the polished surfaces of composites A, B, C, and D are shown in Fig. 1(a-d), respectively. From the figure, we can easily distinguish the zirconia grain (light colored) and the alumina grain (grey colored) due to the atomic number difference. The zirconia particles are well distributed in alumina matrix which could inhibit abnormal grain growth of alumina grains. In addition, based on the microstructure observation in higher magnification factors shown in Fig. 2(a), it is found that some flake-like grains exist in  $Zr^{4+}/La^{3+}$  system, and the EDS characterization of such a grain indicates that is composed the element of O, Al and La. Meanwhile, EDS of the matrix grain indicates that the grain is composed of the element of O and Al (Fig. 2(b)). In order to clarify the phase of the flake-like grains, an XRD test was conducted and shown in Fig. 2(c). The XRD patterns of all sample show that  $Al_2O_3$  and  $t-ZrO_2$  are the major phase, and  $m-ZrO_2$  minor phase, respectively. Moreover, different from the other three sample, a new phase  $LaAl_{11}O_{18}$  occurs in sample A, which corresponds to the flake-like grain in Fig. 2(a). The generation of the  $LaAl_{11}O_{18}$  phase could be explained as follows [19], which could also explain the high intensity of  $m-ZrO_2$  in sample A.



In addition, the microstructure of  $Zr^{4+}/La^{3+}$  system is very dense without obvious pores, which could be further proved by the typical TEM image shown in Fig. 2(d). The weights increase, average grain size, density, relative density and Vickers hardness of the four researched systems combined with the referenced pure alumina and ZTA are listed in Table 1. It can be seen that the alumina grain growth is effectively inhibited after infiltration (from 2.21  $\mu m$  to less than 1  $\mu m$ ). It can also be observed that the densities of all the infiltrated samples which are above 99% are higher than that of the sintered samples which has not been subjected to infiltration (96.21%). However, although the densities of the samples subjected to infiltration increased, considering the introduction of zirconia and the hardness of zirconia is lower than that of alumina, the hardness of all the composites subjected to the infiltration treatment are not much higher than the pure alumina.

The crack resistance as a function of the crack size of the  $Zr^{4+}/La^{3+}$  system is shown in Fig. 3 (a). The fracture toughness of Sample B, C, and D remained basically unchanged versus the crack size, the phenomenon of which is common in brittle materials. However, it can be seen that the fracture toughness of sample A increased with the increase of the crack size. Herein, the toughness of the composites can be divided into three parts using the following equation [20, 21]

$$K_{IC}^C = K_{IC}^m + \Delta K_{IC}^z + \Delta K_{IC}^l \quad (3)$$

Where  $K_{IC}^m$  is fracture toughness of the  $Al_2O_3$  matrix,  $\Delta K_{IC}^z$  is the contribution from the  $ZrO_2$ , and  $\Delta K_{IC}^l$  is the contribution from the  $LaAl_{11}O_{18}$  platelets. As can be seen in XRD, only a little  $m-ZrO_2$  exist in sample B, C, and D. The intensity of  $m-ZrO_2$  phase is higher than that in B, C and D while the fracture toughness of

Sample A is higher than the other four, which illustrate the effect of phase transformation toughen mechanism is small for Sample A. Hence, to understand the enhanced  $\Delta K_{Ic}$ , we can focus on the residual stress caused by thermal expansion misfit. The global residual stress of composites can also be computed as following equations [22].

$$\sigma_m = (\alpha_m - \alpha_l) \left[ \frac{1-2\nu_m}{E_m} + \frac{1+f_m+\nu_l(1-4f_m)}{2E_l(1-f_m)} \right]^{-1} \Delta T \quad (4)$$

And,

$$\sigma_l = \frac{f_m}{1-f_m} \sigma_m \quad (5)$$

Where  $\sigma_m$  and  $\sigma_l$  are residual stress in ZTA matrix and  $\text{LaAl}_{11}\text{O}_{18}$  platelets,  $\alpha_m$  and  $\alpha_l$  ( $\alpha_m = 8.7 \times 10^{-6}/\text{K}$ ,  $\alpha_l = 7.7 \times 10^{-6}/\text{K}$ ) are thermal expansion coefficients of ZTA matrix and  $\text{LaAl}_{11}\text{O}_{18}$  platelets, respectively.  $\nu_m$  and  $\nu_l$  are Poisson's ratios of ZTA matrix and  $\text{LaAl}_{11}\text{O}_{18}$  platelets,  $E_m$  and  $E_l$  are Young's modulus of ZTA matrix and  $\text{LaAl}_{11}\text{O}_{18}$  platelets [23],  $f_m$  is the volume fraction of the ZTA matrix,  $\Delta T$  is the difference in temperature over which the stress is locked in. From the calculation of equations above, the residual stress of  $\text{LaAl}_{11}\text{O}_{18}$  versus temperature is shown in Fig. 4(a), and the compressive stress in  $\text{LaAl}_{11}\text{O}_{18}$  platelets is 689 MPa, while the tensile stress of ZTA matrix is 28 MPa. The thermal expansion coefficient differences between  $\text{ZrO}_2$  ( $10.5 \times 10^{-6}/^\circ\text{C}$ ),  $\text{Al}_2\text{O}_3$  ( $8.5 \times 10^{-6}/^\circ\text{C}$ ), and  $\text{LaAl}_{11}\text{O}_{18}$  ( $7.7 \times 10^{-6}/^\circ\text{C}$ ) impose compressive stress on  $\text{Al}_2\text{O}_3$  grain boundaries, which strengthens the grain boundary and leads to more energy consumed when crack passes through flake-like  $\text{LaAl}_{11}\text{O}_{18}$  grains (Fig. 3(b)). As a result, the fracture toughness of the  $\text{Zr}^{4+}/\text{La}^{3+}$  composite system would be tremendously improved [24]. A schematic of the interaction between the propagating crack and the  $\text{LaAl}_{11}\text{O}_{18}$  grain in the presence of highly localized tensile or compressive stresses at  $\text{LaAl}_{11}\text{O}_{18}$  grain surface is shown in Fig. 4(b). It can be noted that since  $\text{LaAl}_{11}\text{O}_{18}$  grain are placed in "hoop-compression", the crack would be attracted to pass through them, and thus result in transgranular fracture. Due to that more fracture work would be drastically consumed when transgranular fracture occurs, the fracture toughness of the  $\text{Zr}^{4+}/\text{La}^{3+}$  system would be thus drastically enhanced. Therefore, the effect of residual stresses on the fracture toughness was confirmed by satisfactory agreement between the theoretical calculation and the crack path characteristics determined experimentally above.

To explore the contribution of residual stress on toughening of ZTA composites, an empirical equation proposed by Ramachandran and Shetty [25] was introduced to describe the measured toughness enhanced behaviors,

$$K_R = K_\infty - (K_\infty - K_0) \exp(-c/\lambda) \quad (6)$$

Where  $K_{\infty}$ ,  $K_0$  and  $\lambda$  are adjusted parameters. In the case of the present ZTA and co-doped ZTA,  $K_0$  is the intrinsic fracture resistance defined as the fracture toughness just to start crack extension in the absence of shielding.  $K_{\infty}$  is the steady-state fracture toughness when a steady-state process zone has been developed behind the crack tip, and  $\lambda$  is a fitting constant while  $c$  is the crack length (the sum of  $a$  and  $l$ ). It can be seen that experimental data can be fit well by Eq. (4). And the values of  $K_0$  and  $K_{\infty}$  were  $5.53 \text{ MPa}\cdot\text{m}^{1/2}$  and  $17.76 \text{ MPa}\cdot\text{m}^{1/2}$ , respectively, which indicate that residual stress contributes a lot to toughening. That is to say, the measured fracture toughness values under the different 4 loads could be fitted as a rising R-curve behavior with the steady-state fracture toughness of  $17.76 \text{ MPa}\cdot\text{m}^{1/2}$ . The enormous enhancement of the crack resistance versus the crack size could be attributed to thermal expansion misfit and flake-like  $\text{LaAl}_{11}\text{O}_{18}$  in the  $\text{Zr}^{4+}/\text{La}^{3+}$  system.

## 4. Conclusions

In summary, we combined liquid precursor infiltration of high introduction amount of bi-additives (20 wt%) and stereolithography-based 3D printing to fabricate zirconia toughened alumina, and the infiltration systems consist of the four following systems  $\text{Zr}^{4+}/\text{La}^{3+}$ ,  $\text{Zr}^{4+}/\text{Er}^{3+}$ ,  $\text{Zr}^{4+}/\text{Gd}^{3+}$ , and  $\text{Zr}^{4+}/\text{Ce}^{4+}$ . The sample immersed with  $\text{Zr}^{4+}/\text{La}^{3+}$  shows intense peaks of  $m\text{-ZrO}_2$  phase compared to the other samples while a new phase of flake-like  $\text{LaAl}_{11}\text{O}_{18}$  occurs in the  $\text{Zr}^{4+}/\text{La}^{3+}$  immersed sample, the existence of which could be confirmed by XRD and EDS. The fracture toughness of the  $\text{Zr}^{4+}/\text{Er}^{3+}$ ,  $\text{Zr}^{4+}/\text{Gd}^{3+}$ , and  $\text{Zr}^{4+}/\text{Ce}^{4+}$  samples remained basically unchanged versus the crack size, while the measured fracture toughness values for the  $\text{Zr}^{4+}/\text{La}^{3+}$  system could be fitted as a rising R-curve behavior with the steady-state fracture toughness of  $17.76 \text{ MPa}\cdot\text{m}^{1/2}$ . The enormous enhancement of the toughness could be attributed to thermal expansion misfit and flake-like  $\text{LaAl}_{11}\text{O}_{18}$  in the  $\text{Zr}^{4+}/\text{La}^{3+}$  system. The effect of residual stresses on the fracture mode and thus the toughness is discussed on the basis of theoretical calculation and analysis. It is the first time a rising R-curve behavior is observed in the 3D printed ceramics. The shocking discovery provides a highly effective toughening way in 3D printing combined infiltration approach.

## Declarations

### Acknowledgements

This work was financially supported by Local Innovative and Research Team Project of Guangdong Pearl River Talents Program (Grant No. 2017BT01C169), the Science and Technology Project of Guangdong Province (Grant Nos. 2016B090915002 and 2017A010103046), National Natural Science Foundation of China (NSFC, Grant No. 51872052 and 91960102), Pearl River S&T Nova Program of Guangzhou (Grant No. 201806010173), and Guangdong Provincial Science Fund for Distinguished Young Scholars (2020B1515020059).

## References

1. Meng FC, Liu C, Zhang F, Tian ZQ, Huang WJ. Densification and mechanical properties of fine-grained  $\text{Al}_2\text{O}_3\text{-ZrO}_2$  composites consolidated by spark plasma sintering. *J Alloy Compd.* 2012;512:63–7.
2. Wu HD, Liu W, He RX, Wu ZW, Jinag QG, Song X, et al. Fabrication of dense zirconia-toughened alumina ceramics through a stereolithography-based additive manufacturing. *Ceram Int.* 2017;43:968–72.
3. Echeberria J, Ollo J, Bocanegra-Bernal MH, Garcia-Reyesc A, Domínguez-Rios C, Aguilar-Elguezabal A, et al. Sinter and hot isostatic pressing (HIP) of multi-wall carbon nanotubes (MWCNTs) reinforced ZTA nanocomposite: Microstructure and fracture toughness. *Int J Refract Metal Hard Mater.* 2010;28:399–406.
4. Wang SK, Yu JY, Li Q, Zheng ER, Duan YG, Qi GC, et al. Preparation of Gradient ZTA Ceramic by Centrifugal Slip Casting Method. *Adv Mater Res.* 2012;569:324–27.
5. Jiménez-Melendo M, Clauss C, Domínguez-Rodríguez A, Portu GD, Roncari E, Pinasco P. High temperature plastic deformation of multilayered YTZP/ZTA composites obtained by tape casting. *Acta Mater.* 1998;46:3995–4004.
6. Gadow R, Kern F. Pressureless Sintering of Injection Molded Zirconia Toughened Alumina Nanocomposites. *J Ceram Soc Jpn.* 2006;114:958–62.
7. Zocca A, Paolo C, Gomes CM, Cynthia, Günster J. Additive Manufacturing of Ceramics: Issues, Potentialities, and Opportunities. *J Am Ceram Soc.* 2015;98:1983–2001.
8. Wu Z, Liu W, Wu H, Huang R, He RX, Jiang QG, et al. Research into the mechanical properties, sintering mechanism and microstructure evolution of  $\text{Al}_2\text{O}_3\text{-ZrO}_2$  composites fabricated by a stereolithography-based 3D printing method. *Mater Chem Phys.* 2018;207:1–10.
9. Zhou M, Liu W, Wu H, Song X, Chen Y, Cheng LX, et al. Preparation of a defect-free alumina cutting tool via additive manufacturing based on stereolithography-Optimization of the drying and debinding processes. *Ceram Int.* 2016;42:11598–602.
10. Tian Z, Yang YP, Wang Y, Wu HD, Liu W, Wu SH. Fabrication and properties of a high porosity h-BN-SiO<sub>2</sub> ceramics fabricated by stereolithography-based 3D printing. *Mater Lett.* 2019;236:144–7.
11. Brinckmann SA, Patra N, Yao J, Ware TH, Frick CP, Fertig RS III. Stereolithography of SiOC Polymer-Derived Ceramics Filled with SiC Micronwhiskers. *Adv Eng Mater.* 2018;20:1800593.
12. Lin JD, Duh JH. Correlation of mechanical properties and composition in tetragonal  $\text{CeO}_2\text{-Y}_2\text{O}_3\text{-ZrO}_2$  ceramic system. *Mater Chem Phys.* 2003;78:246–52.
13. Tomaszewski H, Boniecki M, Weglarz H. Toughness-curve behaviour of alumina-SiC and ZTA-SiC composites. *J Eur Ceram Soc.* 2000;20:1215–24.
14. Becher PH, Alexander KB, Bleier A, Waters SH, Warwick WH. Influence of  $\text{ZrO}_2$  grain size and content on the transformation response in the  $\text{Al}_2\text{O}_3\text{-ZrO}_2$  (12 mol%  $\text{CeO}_2$ ) system. *J Am Ceram Soc.* 1993;76:657–63.

15. Reyes-Rojas A, Dominguez-Rios C, Garcia-Reyes A, Aguilar-Elguezaba A, Bocanegra-Bernal MH. Sintering of carbon nanotube-reinforced zirconia-toughened alumina composites prepared by uniaxial pressing and cold isostatic pressing. *Materials. Research Express*. 2018;5:105602.
16. Zhang F, Vanmeensel K, Inokoshi M, Batuk M, Hadermann J, Meerbeek BW, et al. Critical influence of alumina content on the low temperature degradation of 2–3 mol% yttria-stabilized TZP for dental restorations. *J Eur Ceram Soc*. 2015;35:741–50.
17. Tsukuma K, Shimada M. Strength, fracture toughness and Vickers hardness of CeO<sub>2</sub>-stabilized tetragonal ZrO<sub>2</sub> polycrystals (Ce-TZP). *Journal of Materials Science*. 1985;20:1178–84.
18. Niihara K. A fracture mechanics analysis of indentation-induced Palmqvist crack in ceramics. *Journal of Materials Science Letters*. 1983;2:221–3.
19. Wu YQ, Zhang YF, Wang SW, Guo JK. In-situ synthesis of rodlike LaAl<sub>11</sub>O<sub>18</sub> in Al<sub>2</sub>O<sub>3</sub> powder by a coprecipitation method. *J Eur Ceram Soc*. 2001;21:919–23.
20. Becher PH. Microstructural design of toughened ceramics. *J Am Ceram Soc*. 1991;74:255–69.
21. Wu WW, Gui JY, Zhu TB, Xie ZP. The effect of residual stress on whisker reinforcements in SiCw-Al<sub>2</sub>O<sub>3</sub> composites during cooling. *J Alloy Compd*. 2017;725:639–43.
22. Peterson IM, Tien TY. Effect of the grain boundary thermal expansion coefficient on the fracture toughness in silicon nitride. *J Am Ceram Soc*. 1995;78:2345–52.
23. Jiang B, Fang MH, Huang ZH, Liu YG, Peng P, Zhang J. Mechanical and thermal properties of LaMgAl<sub>11</sub>O<sub>19</sub>. *Mater Res Bull*. 2010;45:1506–8.
24. Naga SM, Hassan AM, El-Maghraby, Awaad HF, Elsayed M. H. In-situ sintering reaction of Al<sub>2</sub>O<sub>3</sub>–LaAl<sub>11</sub>O<sub>18</sub>–ZrO<sub>2</sub> composite. *International Journal of Refractory Metals Hard Materials*. 2016;54:230–6.
25. Ramachandran N, Shetty DK. Rising crack-growth-resistance (R-Curve) behavior of toughened alumina and silicon nitride. *J Am Ceram Soc*. 1991;74:2634–41.
26. Wu HD, Liu W, Huang RJ, He RX, Huang MP, An D, et al. Fabrication of high-performance Al<sub>2</sub>O<sub>3</sub>-ZrO<sub>2</sub> composite by a novel approach that integrates stereolithography-based 3D printing and liquid precursor infiltration. *Materials Chemistry Physics*. 2018;209:31–7.

## Tables

**Table 1** The weights increase, average grain size, density, relative density and Vickers hardness the four researched systems combined with the referenced pure alumina and ZTA

Sample	Zirconia Content (wt%)	Grain Size (µm)	Density (g/cm <sup>3</sup> )	Relative Density	Hardness (GPa)
Pure Alumina[26]	0	2.21	3.81	96.21%	16.99±0.32
A	19.84%	0.84	4.24	99.25%	17.06±0.18
B	19.70%	0.96	4.26	99.89%	17.08±0.36
C	18.59%	0.73	4.23	99.53%	17.32±0.27
D	21.88%	0.83	4.29	99.87%	17.03±0.33
ZTA[2]	20%	0.80	4.27	99.76%	17.42±0.27

## Figures

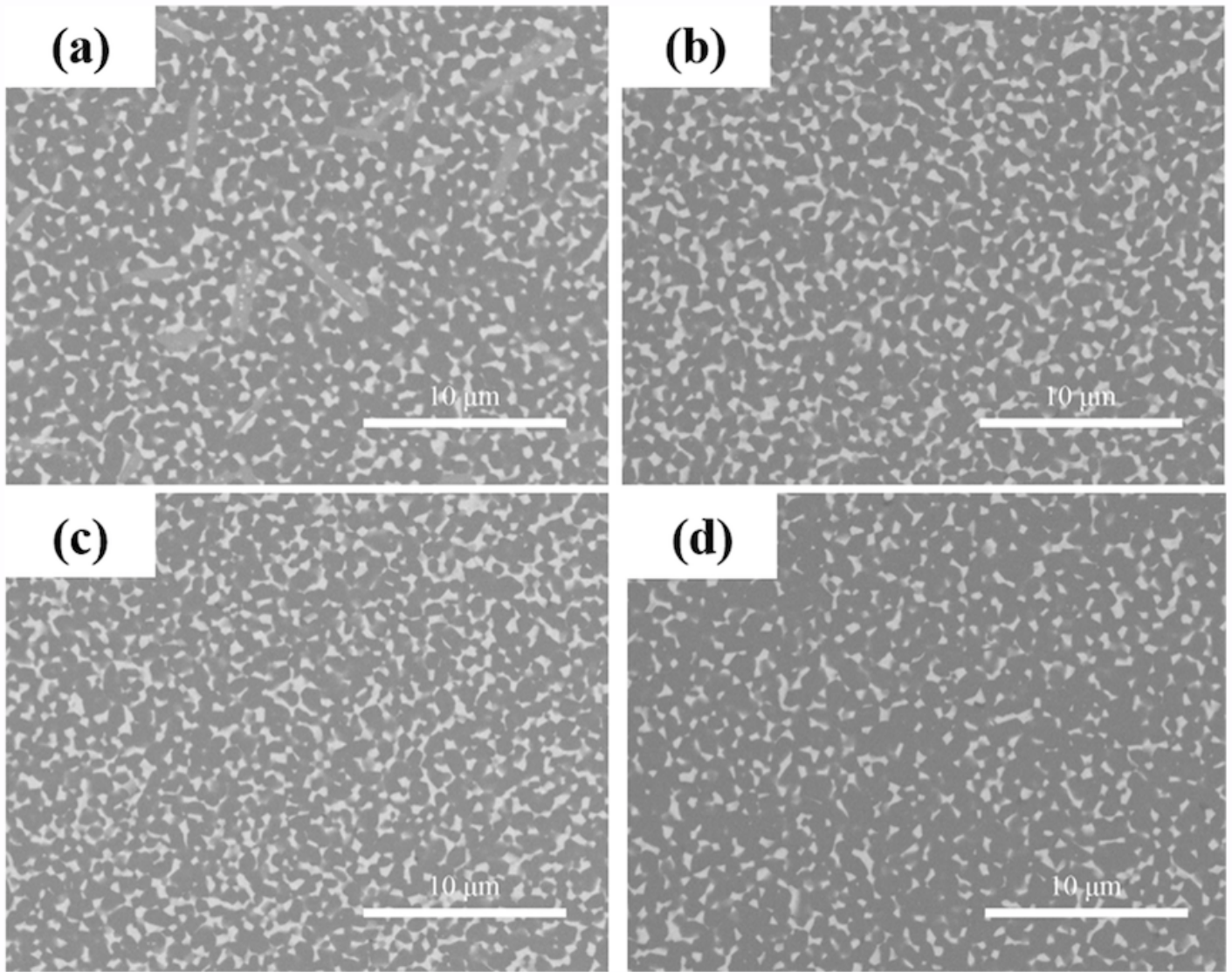


**Figure 1**

(a-d) The respective microstructures of the polished surfaces of composites  $Zr^{4+}/La^{3+}$ ,  $Zr^{4+}/Er^{3+}$ ,  $Zr^{4+}/Gd^{3+}$ ,  $Zr^{4+}/Ce^{4+}$  doped  $Al_2O_3$

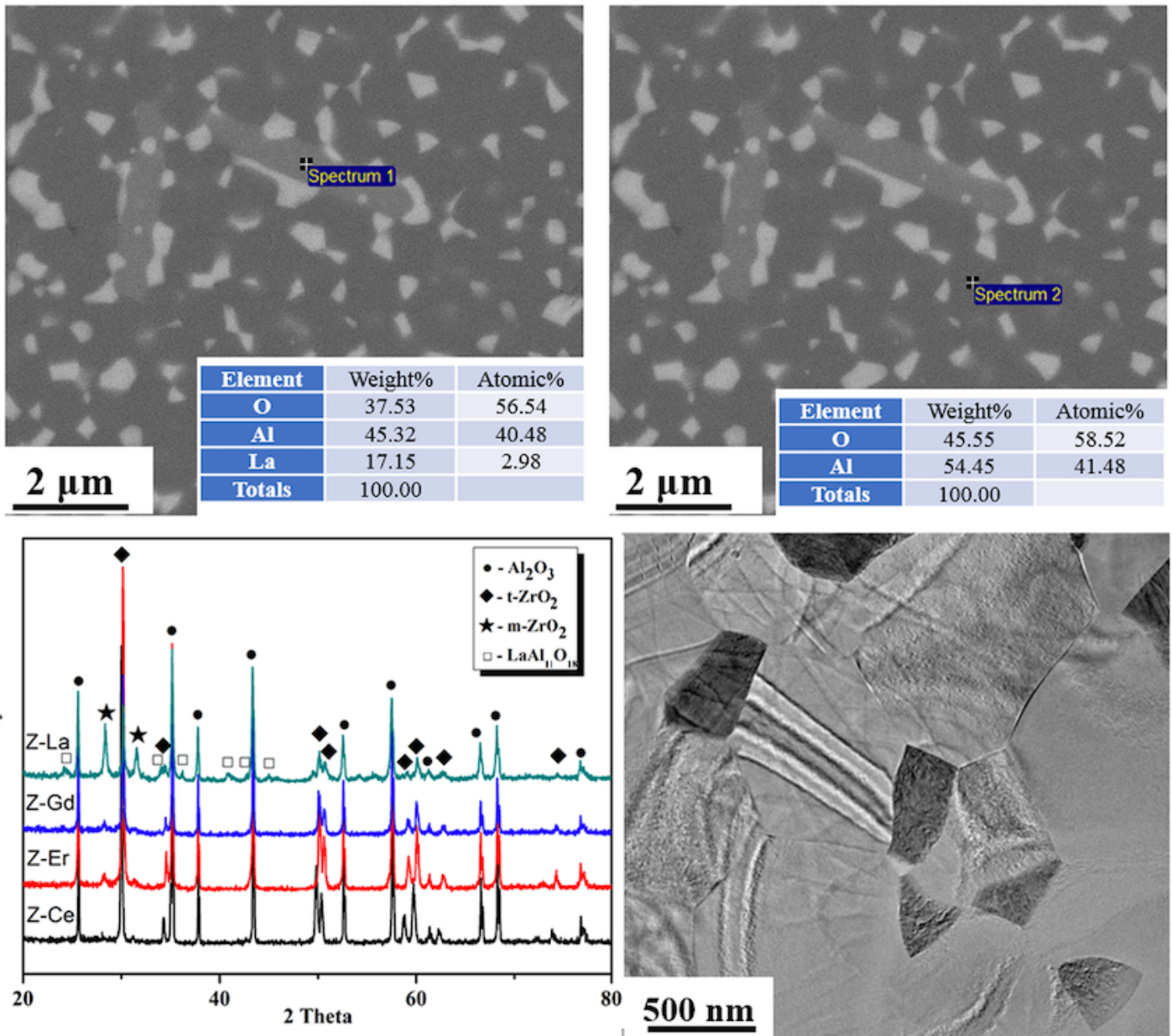


Figure 2

(a, b) SEM images of the  $\text{Zr}^{4+}/\text{La}^{3+}$  system in higher magnification factors and the corresponding EDS analysis; (c) An XRD pattern of the as-prepared  $\text{Zr}^{4+}/\text{La}^{3+}$  co-doped  $\text{Al}_2\text{O}_3$ ; (d) typical TEM image of the  $\text{Zr}^{4+}/\text{La}^{3+}$  co-doped  $\text{Al}_2\text{O}_3$  system

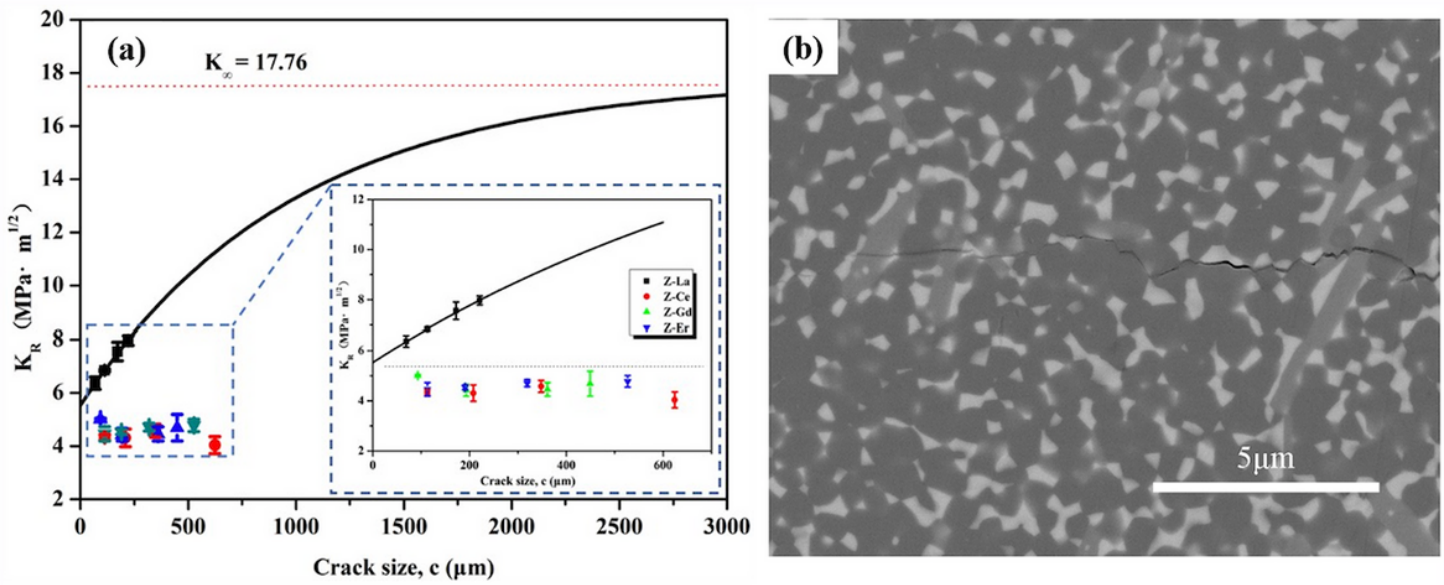


Figure 3

(a) The crack resistance as a function of the crack size of the Zr<sup>4+</sup>/La<sup>3+</sup> system; (b) The crack propagation image passing through LaAl<sub>11</sub>O<sub>18</sub> grains

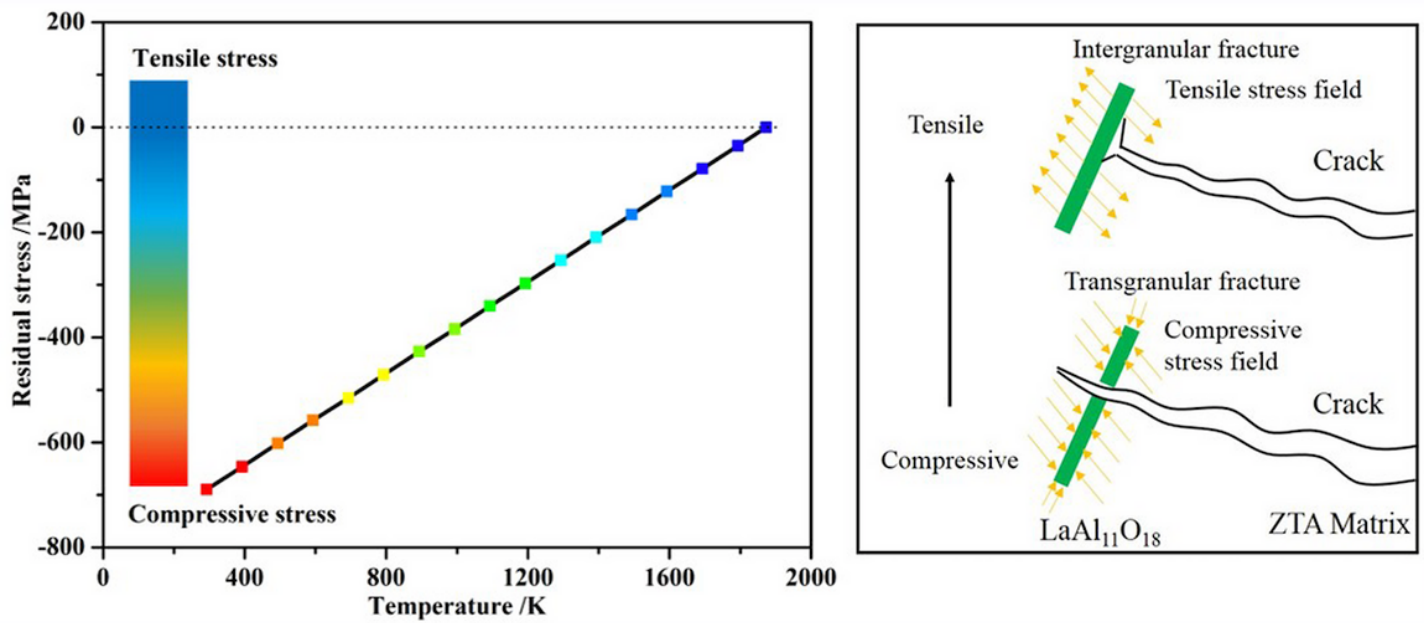


Figure 4

(a) Residual stress calculations for LaAl<sub>11</sub>O<sub>18</sub> grain at temperatures ranging from 293K to 1873 K; (b) The effect of residual stress on the fracture mode of LaAl<sub>11</sub>O<sub>18</sub>